European Radiology (2022) 32:639–649
https://doi.org/10.1007/s00330-021-08134-y

BREAST

Diagnostic performance of perilesional radiomics analysis of contrast-enhanced mammography for the differentiation of benign and malignant breast lesions

Simin Wang[1,2] · Yuqi Sun[3] · Ruimin Li[1,2] · Ning Mao[4] · Qin Li[1,2] · Tingting Jiang[1,2] · Qianqian Chen[5] · Shaofeng Duan[5] · Haizhu Xie[4] · Yajia Gu[1,2]

Received: 24 January 2021 / Revised: 16 May 2021 / Accepted: 1 June 2021 / Published online: 29 June 2021

Abstract

Objective To conduct perilesional region radiomics analysis of contrast-enhanced mammography (CEM) images to differentiate benign and malignant breast lesions.

Methods and materials This retrospective study included patients who underwent CEM from November 2017 to February 2020. Lesion contours were manually delineated. Perilesional regions were automatically obtained. Seven regions of interest (ROIs) were obtained for each lesion, including the lesion ROI, annular perilesional ROIs (1 mm, 3 mm, 5 mm), and lesion + perilesional ROIs (1 mm, 3 mm, 5 mm). Overall, 4,098 radiomics features were extracted from each ROI. Datasets were divided into training and testing sets (1:1). Seven classification models using features from the seven ROIs were constructed using LASSO regression. Model performance was assessed by the AUC with 95% CI.

Results Overall, 190 women with 223 breast lesions (101 benign; 122 malignant) were enrolled. In the testing set, the annular perilesional ROI of 3-mm model showed the highest AUC of 0.930 (95% CI: 0.882–0.977), followed by the annular perilesional ROI of 1 mm model (AUC = 0.929; 95% CI: 0.881–0.978) and the lesion ROI model (AUC = 0.909; 95% CI: 0.857–0.961). A new model was generated by combining the predicted probabilities of the lesion ROI and annular perilesional ROI of 3-mm models, which achieved a higher AUC in the testing set (AUC = 0.940).

Conclusions Annular perilesional radiomics analysis of CEM images is useful for diagnosing breast cancers. Adding annular perilesional information to the radiomics model built on the lesion information may improve the diagnostic performance.

Key Points

- *Radiomics analysis of the annular perilesional region of 3 mm in CEM images may provide valuable information for the differential diagnosis of benign and malignant breast lesions.*
- *The radiomics information from the lesion region and the annular perilesional region may be complementary. Combining the predicted probabilities of the models constructed by the features from the two regions may improve the diagnostic performance of radiomics models.*

Keywords Mammography · Breast cancer · Machine learning

Simin Wang and Yuqi Sun contributed equally to this work.

✉ Yajia Gu
guyajia@126.com

[1] Department of Radiology, Fudan University Shanghai Cancer Center, Shanghai 200032, China

[2] Department of Oncology, Shanghai Medical College, Fudan University, Shanghai 200032, China

[3] Department of Biostatistics, School of Public Health, Fudan University, Shanghai 200032, China

[4] Department of Radiology, Yantai Yuhuangding Hospital, Qingdao University, Shandong 264000, China

[5] GE Healthcare China, No. 1 Huatuo Road, Shanghai 210000, China

Abbreviations

ADC	Apparent diffusion coefficient
AJCC	American Joint Committee on Cancer
AUC	Area under the ROC curve
BC	Breast cancer
BI-RADS	Breast Imaging Reporting and Data System
CC	Craniocaudal
CEM	Contrast-enhanced mammography
CI	Confidence interval
DES	Dual-energy subtraction
GLCM	Gray-level co-occurrence matrix
GLRLM	Gray-level run length matrix
GLSZM	Gray-level size zone matrix
HE	High energy
ICC	Intraclass correlation coefficient
LASSO	Least absolute shrinkage and selection operator
LE	Low energy
MLO	Mediolateral oblique
MRI	Magnetic resonance imaging
ROC	Receiver operating characteristic
ROI	Region of interest
SD	Standard deviation
SLN	Sentinel lymph node
TIL	Tumor-infiltrating lymphocyte

Background

Contrast-enhanced mammography (CEM) is an emerging breast imaging technology [1–3]. Based on the dual-energy mammographic technique, it utilizes intravenous injection of iodinated contrast material to depict the contrast-enhanced area of breast lesions [4, 5]. Breast cancers (BCs) can be detected on CEM with high sensitivity due to the neovascularity associated with malignancy [6, 7], even in women with dense breasts [8–10].

With the advances of computer technology, radiomics has been developing rapidly. Radiomics utilizes high-throughput computing to extract a large number of image features and converts standard-of-care medical images into quantifiable data, which can subsequently be analyzed using conventional biostatistics and artificial intelligence, including machine learning methods [11, 12]. Some previous studies utilized radiomics analysis in the diagnosis of BC and showed promising results [13–18]. However, these studies solely focused on the extent of the tumor. The immediate surrounding tumor environment or the bulk parenchyma around the tumor has remained unexplored thus far.

With increasing interest in the tumor microenvironment in recent decades, there has been a growing body of research focusing on the quantitative characterization of the surrounding peripheral areas of tumors, since this area is related to the blood and lymphatic plexus, immune infiltration, and stromal response [19–23] and may contribute to risk factors determining tumor formation [24]. Considering the unique biological significance of the peritumoral region, several recent studies have tried to explore the role of the peritumoral radiomics features of BC and have shown promising results for these features in predicting diagnosis [25–28] or prognosis [29, 30], as well as in reflecting intrinsic biological factors and the therapeutic response of BC [31, 32]. However, these studies employed breast magnetic resonance imaging (MRI) or ultrasound images, and no studies so far have used the perilesional radiomics features in CEM images for the diagnosis of BC.

Therefore, the main goal of this study was to evaluate whether radiomics analysis of the perilesional region in CEM images can contribute to the differentiation between benign and malignant breast lesions. Furthermore, we intended to explore which range of the perilesional region may provide the most valuable diagnostic information.

Methods and materials

Study subjects

We retrospectively collected data from consecutive female patients who underwent CEM from November 2017 to February 2020. The inclusion criteria were as follows: (1) patients with suspected breast lesions after physical examination, mammography screening, or ultrasound; (2) patients who were referred for CEM as part of diagnostic imaging; and (3) patients with pathological results of the lesions. We excluded patients (1) with missing data; (2) with a history of breast surgery, breast radiotherapy, chemotherapy, or hormone treatment within 6 months prior to CEM examination; and (3) with poor image quality. According to the American Joint Committee on Cancer (AJCC) Cancer Staging Manual (Eighth Edition), lobular carcinoma in situ is a benign entity. Therefore, we excluded it in the subsequent analysis (n = 1). The patient inclusion and exclusion criteria are shown in Figure 1. The Institutional Review Board and Ethics Committee approved this study. The requirement for written informed consent was waived.

CEM examination

All CEM examinations were performed using the Senographe Essential mammography system (GE Healthcare). First, all patients received an intravenous injection of the contrast material (Iohexol, 350 mg I/mL) at a dose of 1.5 mL/kg and at a rate of 3 mL/s. A 20-mL saline bolus was administered immediately before and after contrast injection. Two minutes after contrast injection, images were obtained in the following order: craniocaudal (CC) and mediolateral oblique (MLO) views of the suspicious breast and then CC and MLO views

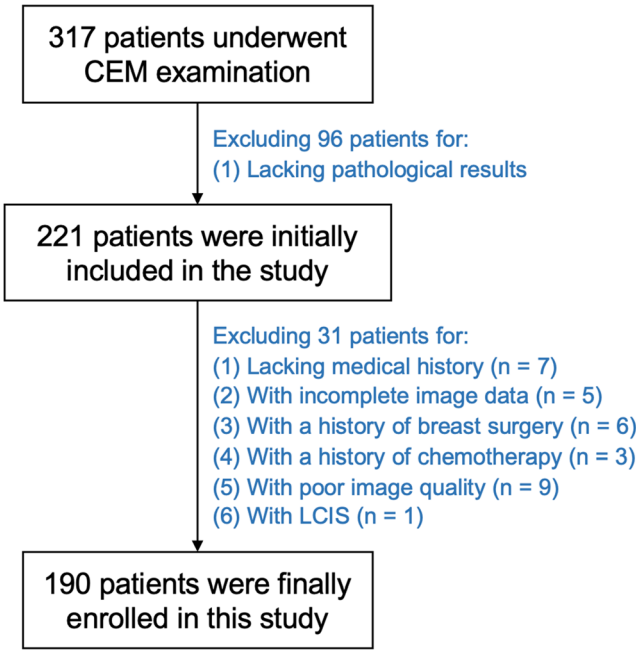

Figure 1 Patient inclusion and exclusion criteria. CEM = contrast-enhanced mammography; LCIS = lobular carcinoma in situ

of the less suspicious breast. For each mammographic projection, a pair of high-energy (HE) and low-energy (LE) exposures were consecutively performed to obtain HE and LE images, and a dual-energy subtraction (DES) image was generated automatically with the mammography unit by using a dual-energy weighted logarithmic subtraction technique.

CEM image evaluation

All CEM images were reviewed by two radiologists (reader 1: 4 years of experience in breast imaging; reader 2: 10 years of experience in breast imaging). They were informed of the location of each lesion but were blinded to the clinical and pathological information of the patients. They evaluated the basic characteristics of the patients, including breast density, lesion enhancement degree, and degree of background parenchymal enhancement with reference to the Breast Imaging Reporting and Data System (BI-RADS) lexicons for mammography and MRI [33], considering that these indexes may affect the performance of the radiomics analysis. In the case of a discrepancy, the final decision was made in consensus. The largest diameters of the lesions were measured independently by the two radiologists in CC view images. The mean values were calculated as the final lesion sizes. The diagnostic performance of the human readers in the use of CEM images is provided in Appendix E1.

Reference standard

The standard of reference was the histopathologic diagnosis obtained by biopsy or surgery within 1 month after CEM examination. Malignant cases were defined as lesions that contained any invasive components or ductal carcinoma in situ. Benign cases were defined as lesions that did not contain any invasive components or carcinoma in situ. The definitions of molecular subtypes of malignant lesions are provided in Appendix E2.

Image segmentation

The image segmentation process included lesion segmentation and perilesional region segmentation. All segmentation steps were performed in the CC and MLO views of the HE, LE, and DES images. The detailed lesion delineation methods are listed in Appendix E3. The diagram and examples of the image segmentation scheme are shown in Figure 2.

First, radiologist 1 (3 years of experience in breast imaging) reviewed the CEM images and indicated the location of each lesion with reference to the pathological report. Then, based on the information, radiologist 2 (5 years of experience) manually delineated the contours of the lesions by using ITK-SNAP (version 3.6; *www.itksnap.org*) software [34]. All the contours were reviewed and agreed upon by radiologist 3 (8 years of experience).

Annular perilesional regions (not containing the lesion area) of 1 mm, 3 mm, and 5 mm were obtained automatically by dilating the delineated lesion contours using Spectral Mammography Kit (SMK) software (version 1.2.0, GE Healthcare). A morphologic dilation operation was performed to capture the perilesional region [35]. If the contours of perilesional regions were beyond the parenchyma of the breast after expansion, the portion beyond the parenchyma was manually removed.

In addition, we defined another three regions of interest (ROIs), which include both the lesion area and the surrounding perilesional area (1 mm, 3 mm, and 5 mm) within the same ROI.

Finally, for each lesion in each image, a total of seven ROIs, namely, lesion ROI (L), annular perilesional ROIs of 1, 3, and 5 mm (P1, P3, and P5), lesion + perilesional ROIs of 1, 3, and 5 mm (LP1, LP3, and LP5), were generated to extract radiomics features.

Radiomics feature extraction

Before radiomics feature extraction, image preprocessing, including image resampling and gray level discretization, was performed. The image preprocessing and radiomics feature extraction procedures were conducted by using SMK software. All voxel sizes of all images were resampled to the same size of 0.2 mm × 0.2 mm. The image gray level was discretized to a scale of 0 to 255. For each ROI in each image, a total of 680 features, including 18 first-order features, 14 shape features, 24 Gray-level co-occurrence matrix (GLCM)

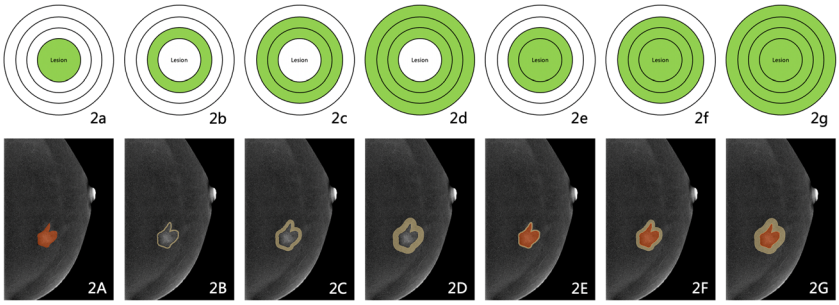

Figure 2 (2a–2g) Schematic illustration of the lesion and perilesional regions of interest (ROIs) and (2A–2G) examples of the image segmentation scheme. The lesion shown in the dual-energy subtraction (DES) images of contrast-enhanced mammography (CEM) was pathologically proven to be invasive ductal carcinoma (grade II). The radiomics features were extracted from the seven ROIs. (2a, 2A) Lesion ROI (L). (2b, 2B) Annular perilesional ROI of 1 mm (P1). (2c, 2C) Annular perilesional ROI of 3 mm (P3). (2d, 2D) Annular perilesional ROI of 5 mm (P5). (2e, 2E) Lesion + perilesional ROI of 1 mm (LP1). (2f, 2F) Lesion + perilesional ROI of 3 mm (LP3). (2g, 2G) Lesion + perilesional ROI of 5 mm (LP5)

features, 16 Gray-level size zone matrix (GLSZM) features, 16 Gray-level run length matrix (GLRLM) features, and 592 wavelet features, were extracted. Since there were a total of 6 images for each ROI (HE-CC, HE-MLO, LE-CC, LE-MLO, DES-CC, and DES-MLO), a total of 4,080 radiomics features were extracted from each ROI (L, P1, P3, P5, LP1, LP3, and LP5).

Intraobserver and interobserver agreement

The intraclass correlation coefficient (ICC) was used to evaluate the reproducibility of manual radiomics feature extraction. Three months later, two radiologists (radiologist 2 and radiologist 3) randomly selected 30 patients and repeated the segmentation process. The intraobserver and interobserver ICCs were calculated. The radiomics features with ICCs greater than 0.75 were considered to have good agreement and were retained for the following feature selection procedure.

Feature selection and radiomics model construction

A total of seven radiomics models were constructed to differentiate malignant lesions from benign lesions by using the feature datasets from the seven ROIs (Figure 3). Each dataset was divided into training and testing sets at a ratio of 1:1 using the stratified random sampling method based on age. The training set was further divided into training and validation subsets. Each of the three sets was independent, without any overlap [36]. The training subset was used to build the models and the training algorithm was tuned and validated on the validation subset [37]. The testing set, which was not involved in model construction or parameter tuning, was used to assess the performance of the model.

Least absolute shrinkage and selection operator (LASSO) regression [38] with 10-fold cross-validation was used to determine the best subsets of predictive features and to construct the radiomics models based on the features derived from each ROI. The radiomics signature score was calculated for each lesion by using a linear combination of the values of the selected features weighted by their respective coefficients. Areas under the receiver operating characteristic (ROC) curve (AUCs) with 95% confidence intervals (CIs) were used to evaluate the performance of all the models. The DeLong test [39] was used to compare the AUCs of different models. Specifically, we constructed an additional logistic model (model 8) by combining the predicted probabilities calculated from the model constructed using the features from the lesion ROI (model 1) and the model constructed using the features from the annular perilesional ROI that showed the highest AUC value (one of models 2–4) to explore whether the classification performance could be improved.

To illustrate the stability and robustness of the performance of the models, all data were randomly re-split into training and testing sets at a ratio of 1:1 100 times. The same model construction procedure as previously mentioned was used each time of splitting to construct radiomics models for each ROI. Therefore, 100 AUC values for each radiomics model were obtained for evaluation, and the mean values ± standard deviations (SDs) of the 100 AUCs were calculated.

Statistical analysis

All statistical analyses were performed using R (version 3.6.2; www.r-project.org). LASSO regression and ROC curve analyses were conducted using the glmnet and pROC packages. Aside from the radiomics analysis, the chi-square test or Fisher's exact test was used to compare the differences in categorical variables, whereas the two-sample t test was utilized to compare the differences in continuous variables. The Wilcoxon rank-sum test with Bonferroni correction and the Kruskal-Wallis rank-sum test were used to compare the mean AUCs of each kind of ROI in the re-splitting analysis. A two-sided p value of less than 0.05 was considered statistically significant.

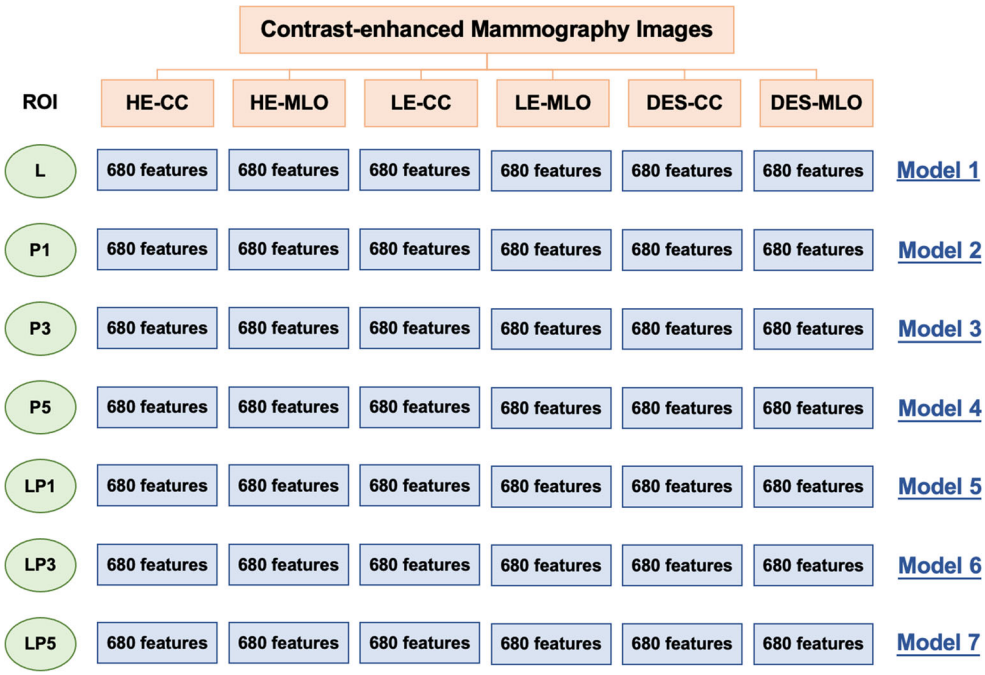

Figure 3 Seven radiomics models were constructed by using the feature datasets from the seven regions of interest (ROIs). Model 1 (L): lesion ROI. Model 2 (P1): annular perilesional ROI of 1 mm. Model 3 (P3): annular perilesional ROI of 3 mm. Model 4 (P5): annular perilesional ROI of 5 mm. Model 5 (LP1): lesion + perilesional ROI of 1 mm. Model 6 (LP3): lesion + perilesional ROI of 3 mm. Model 7 (LP5): lesion + perilesional ROI of 5 mm. HE = high-energy; LE = low-energy; DES = dual-energy subtraction; CC = craniocaudal; MLO = mediolateral oblique

Results

Patient and lesion characteristics

A total of 190 patients with 223 breast lesions (benign lesions: 101/223, 45.3%; malignant lesions: 122/223, 54.7%) were included in the study. The basic patient and lesion characteristics are provided in Table 1. The median age was 48 years (range, 23–70 years). The median lesion size was 20.5 mm (range, 7.0–109.0 mm). In both the training and testing sets, age, lesion size, lesion enhancement degree, and degree of background parenchymal enhancement were significantly different between the benign and malignant groups (all $p < 0.05$). Details on the histopathological results of the lesions are shown in Table 2.

Performance of the radiomics models

The intraobserver ICC calculated based on the features extracted twice by the same radiologist (radiologist 2) ranged from 0.788 to 0.923. The interobserver ICC of feature extraction obtained by the two radiologists (radiologist 2 and radiologist 3) ranged from 0.770 to 0.901. The results showed good reproducibility of manual radiomics feature extraction.

The performance metrics of the classification models constructed by the radiomics features extracted from the seven ROIs (Figure 2) are shown in Figure 4 and Table 3. The selected radiomics features and their coefficients are shown in Appendix E4.

The performance of the models constructed by the features from either the lesion ROI (Table 3: model 1) or the annular perilesional ROI (Table 3: models 2–4) was good, with all AUCs greater than 0.900 in the testing set. Among all the models, model 3 constructed by the features from the annular perilesional ROI of 3 mm achieved the highest AUCs in both the training and testing sets (AUC = 0.990 in the training set; AUC = 0.930 in the testing set), followed by model 2 constructed by the features from the annular perilesional ROI of 1 mm (AUC = 0.986 in the training set; AUC = 0.929 in the testing set). In the testing set, the performance of model 1 constructed by the features from the lesion ROI and model 4 constructed by the features from the annular perilesional ROI of 5 mm was similar (AUCs = 0.909 and 0.910 for model 1 and model 4, respectively).

However, all the models constructed by the features from the lesion + perilesional ROI (Table 3: models 5–7) did not show satisfactory performance, with all AUCs lower than 0.900 in the testing set (AUC = 0.871, 0.867 and 0.883 for models 5–7, respectively).

In Figure 5, model 8 constructed by combining model 1 (L) and model 3 (P3) achieved significantly higher AUCs in the testing set (AUC = 0.940, all $p < 0.05$).

After re-splitting the whole dataset 100 times, the mean AUC values for all models were obtained and are shown in Figure 6 and Table 4. Among the 7 models constructed by radiomics features from the original 7 ROIs (Table 4: models 1–7), model 3 (P3) still yielded the best overall performance in the testing set (mean AUC = 0.940 ± 0.018), followed by model 2 (P1), model 1 (L), and model 4 (P5), with mean AUCs of 0.936 ± 0.019, 0.930 ± 0.021, and 0.929 ± 0.018, respectively. After combining model 1 (L) and model 3 (P3), model 8 obtained the highest mean AUC value of 0.967 ±

Table 1 Patient and lesion characteristics

Characteristics	Total (n = 223)	Training dataset (n = 112)			Testing dataset (n = 111)		
		Benign (n = 52)	Malignant (n = 60)	*p* value	Benign (n = 49)	Malignant (n = 62)	*p* value
Age, years*	47.4 ± 10.1	44.2 ± 8.5	50.5 ± 7.9	0.0004	42.0 ± 10.7	51.3 ± 10.1	< 0.0001
Lesion size, mm*	24.8 ± 15.8	20.5 ± 14.4	30.3 ± 19.5	0.0002	18.7 ± 13.6	28.1 ± 11.6	< 0.0001
Breast density				0.4593			0.2899
Category a	7/223 (3.1%)	2/52 (3.8%)	1/60 (1.7%)		1/49 (2.0%)	3/62 (4.8%)	
Category b	48/223 (21.5%)	9/52 (17.3%)	15/60 (25.0%)		7/49 (14.3%)	17/62 (27.4%)	
Category c	109/223 (48.9%)	25/52 (48.1%)	32/60 (53.3%)		25/49 (51.0%)	27/62 (45.5%)	
Category d	59/223 (26.5%)	16/52 (30.8%)	12/60 (20.0%)		16/49 (32.7%)	15/62 (24.2%)	
Lesion enhancement degree				< 0.0001			< 0.0001
Minimal	18/223 (8.1%)	6/52 (11.5%)	0/60 (0.0%)		11/49 (22.4%)	1/62 (1.6%)	
Mild	78/223 (35.0%)	26/52 (50.0%)	13/60 (21.7%)		24/49 (49.0%)	15/62 (24.2%)	
Moderate	43/223 (19.3%)	6/52 (11.5%)	14/60 (23.3%)		4/49 (8.2%)	19/62 (30.6%)	
Marked	84/223 (37.7%)	14/52 (26.9%)	33/60 (55.0%)		10/49 (20.4%)	27/62 (43.5%)	
Degree of BPE				0.0492			0.0289
Minimal	74/223 (33.2%)	14/52 (26.9%)	21/60 (35.0%)		15/49 (30.6%)	24/62 (38.7%)	
Mild	70/223 (31.4%)	12/52 (23.1%)	22/60 (36.7%)		11/49 (22.4%)	25/62 (40.3%)	
Moderate	44/223 (19.7%)	14/52 (26.9%)	12/60 (20.0%)		10/49 (20.4%)	8/62 (12.9%)	
Marked	35/223 (15.7%)	12/52 (23.1%)	5/60 (8.3%)		13/49 (26.5%)	5/62 (8.1%)	

*Data are shown as the mean values ± standard deviations. Other data are shown as proportions with percentages in parentheses

The chi-square test or Fisher's exact test was used to compare the differences in breast density, lesion enhancement degree, and degree of BPE, whereas the two-sample t test was used to compare the differences in age and lesion size. A *p* value of less than 0.05 was considered statistically significant

BPE background parenchymal enhancement

0.013 in the testing set. Similarly, models 5–7 (LP1, LP3, and LP5) showed the lowest mean AUCs, with all mean AUCs lower than 0.910.

Discussion

Our study obtained three main results. First, annular perilesional radiomics analysis of CEM images is useful for diagnosing BCs, and an annular perilesional region of 3 mm in CEM images may provide the most valuable information (Table 4: models 2–4). Second, adding annular perilesional information to the radiomics model built on the lesion information may improve the diagnostic performance (Table 4: model 8). Third, when the lesion and perilesional regions were delineated in the same ROI, the models consistently failed to achieve satisfactory diagnostic performance (Table 4: models 5–7).

In recent years, the area surrounding the lesion has attracted increasing interest in radiological studies of BC [25–32], but most studies have focused on MRI or ultrasound images. Some radiomics analyses of CEM images have focused on the tumor itself [13–18, 40–43]. Therefore, it remains unclear what kind of role perilesional radiomics features in CEM images may play in the diagnosis of BCs.

It is known that biological changes in the microenvironment of BCs, such as lymphovascular invasion [44, 45], lymphocytic infiltration [22], collagen deposition [46], and peritumoral edema [47], play an important role in the growth, proliferation, and invasion of tumors [48, 49]. Benign and malignant lesions differ in the properties of their cellular microenvironment. Therefore, the image features of the tissues immediately surrounding BC lesions and other benign lesions may be different. However, the contribution of the microenvironment is not considered in routine radiological diagnostic examinations.

In our study, the model constructed by the features from the annular perilesional region of 3 mm showed good overall classification performance (mean AUC = 0.940). For the differentiation of benign and malignant breast lesions, Zhou et al [25] used a deep learning method and achieved the highest diagnostic accuracy of 89% in the testing set

Table 2 Histopathological results of the lesions

Lesion types	Total
Histological types of benign lesions	101/101 (100.0)
Fibroadenoma	41/101 (40.6)
Adenosis	37/101 (36.6)
Intraductal papilloma	15/101 (14.9)
Inflammation	5/101 (5.0)
Phyllodes tumor	2/101 (2.0)
Tubular adenoma	1/101 (1.0)
Histological types of malignant lesions	122/122 (100.0)
Invasive ductal carcinoma	106/122 (86.9)
Ductal carcinoma in situ	6/122 (4.9)
Invasive lobular carcinoma	3/122 (2.5)
Papillary carcinoma	3/122 (2.5)
Mucinous adenocarcinoma	2/122 (1.6)
Metaplastic carcinoma	1/122 (0.8)
Paget's disease	1/122 (0.8)
Molecular subtypes of malignant lesions*	122/122 (100.0)
Luminal A	33/122 (27.0)
Luminal B/HER2-negative	34/122 (27.9)
Luminal B/HER2-positive	15/122 (12.3)
HER2-positive	19/122 (15.6)
Triple-negative	18/122 (14.8)
Unknown	3/122 (2.5)

Data are shown as proportions with percentages in parentheses

*The definitions of molecular subtypes of malignant lesions are provided in Appendix E2

HER2 human epidermal growth factor receptor 2

when taking proximal peritumor tissue into consideration, which was higher than that of using a tumor ROI alone. Zhou et al suggested that the stiffness of the tissue surrounding malignant breast lesions was higher than that of benign lesions [50]. In our study, after combining the intralesional and annular perilesional radiomics features, the diagnostic performance improved. This is probably because integrating the two kinds of information can reveal the characteristics of the lesions more comprehensively. We also proved that the radiomics features should be separately extracted from the intralesional and annular perilesional areas instead of placing the two regions within the same ROI.

The definitions and segmentation methods of the perilesional region are not exactly the same among different studies. Shin et al [51] employed a shell-based method and found that the apparent diffusion coefficient (ADC) values of the proximal peritumoral stroma (1.18 to 3.54 mm) can discriminate between low-risk and non-low-risk BCs. Fan et al [52, 53] applied a similar segmentation method to predict molecular subtypes and differentiate between low and high Ki-67 BC groups. Braman et al [31, 32] used a circular peritumoral region to estimate the response to neoadjuvant therapy. In our study, the annular expansion method of the perilesional area was similar. Other studies used a rectangular perilesional ROI [25, 26], delineated the peritumoral edema area [54], or employed an isotropic volumetric expansion method [55].

Zhou et al [25] reported that the AUCs decreased with increasing perilesional range in the diagnosis of BCs. Our study also showed that the annular perilesional region of 5 mm did not show satisfactory diagnostic performance compared to the annular perilesional region of 3 mm (mean AUC = 0.940 vs. 0.929). This is probably because as the area around the lesion expands, more potential normal breast tissue was included and may therefore reduce the diagnostic efficacy of the proximal perilesional area immediately surrounding the lesion. However, Kim et al [56] found that the K_{trans} measured in normal-appearing fibroglandular tissue can be used to distinguish between malignant and nonmalignant groups. Li et al [57] also found that the normal parenchyma may provide use-

Table 3 The performance of the radiomics models

Radiomics models	AUC (95% CI)	
	Training set	Testing set
Model 1: lesion (L)	0.979 (0.959, 0.998)	0.909 (0.857, 0.961)
Model 2: annular perilesional ROI of 1 mm (P1)	0.986 (0.971, 1.000)	0.929 (0.881, 0.978)
Model 3: annular perilesional ROI of 3 mm (P3)	0.990 (0.976, 1.000)	0.930 (0.882, 0.977)
Model 4: annular perilesional ROI of 5 mm (P5)	0.984 (0.965, 1.000)	0.910 (0.852, 0.968)
Model 5: lesion + perilesional ROI of 1 mm (LP1)	0.980 (0.962, 0.998)	0.871 (0.806, 0.936)
Model 6: lesion + perilesional ROI of 3 mm (LP3)	0.940 (0.899, 0.980)	0.867 (0.801, 0.933)
Model 7: lesion + perilesional ROI of 5 mm (LP5)	0.939 (0.894, 0.985)	0.883 (0.820, 0.947)

AUC area under the receiver operating characteristic curve, *CI* confidence interval

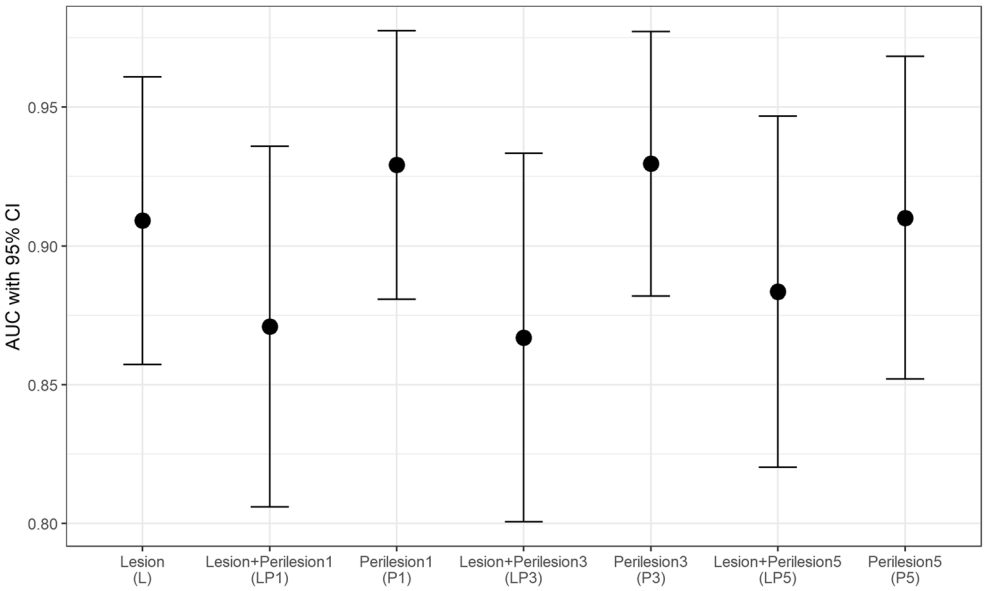

Figure 4 Areas under the receiver operating characteristic curve (AUCs) with 95% confidence intervals (CIs) of the seven radiomics models in the testing set. Model 1 (L): lesion ROI. Model 2 (P1): annular perilesional ROI of 1 mm. Model 3 (P3): annular perilesional ROI of 3 mm. Model 4 (P5): annular perilesional ROI of 5 mm. Model 5 (LP1): lesion + perilesional ROI of 1 mm. Model 6 (LP3): lesion + perilesional ROI of 3 mm. Model 7 (LP5): lesion + perilesional ROI of 5 mm

ful information in a prediction model of BCs. In our study, the diagnostic performance of the annular perilesional ROI of 1 mm was also lower than that of the annular perilesional ROI of 3 mm (mean AUC = 0.940 vs. 0.936). This is probably because although this area immediately surrounds the lesion, it is too small to contain sufficient information to predict BCs. There is no established consensus on the definition of the cutoff distance to distinguish the lesion-related perilesional area from normal breast tissue. Therefore, whether the 3 mm area around the lesion is most suitable for the diagnosis of BCs still needs to be verified by a larger sample. Only one study systematically explored the performance of different peritumoral region sizes in predicting sentinel lymph node (SLN) status in BCs and found that a peritumoral region of 2–4 mm may better predict SLN metastasis [58]. Furthermore, the suitable perilesional area range may also be related to the mean size of the lesions in this study. Delineating the perilesional area in proportion to the size of the lesion may also be a feasible segmentation method.

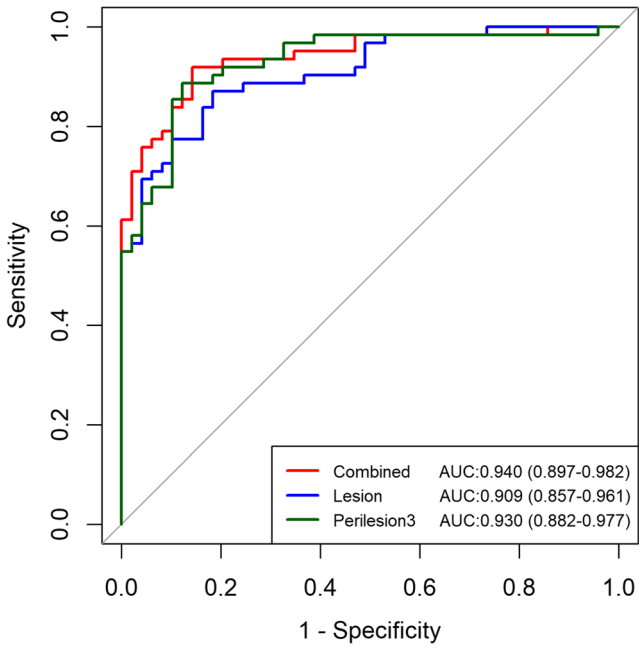

Figure 5 The receiver operating characteristic (ROC) curves. The blue curve represents the ROC curve of the model (model 1) constructed by using the radiomics features extracted from the lesion region of interest (ROI). The green curve represents the ROC curve of the model (model 3) constructed by using the radiomics features extracted from the annular perilesional ROI of 3 mm. The red curve represents the ROC curve of the combined model (model 8) constructed by combining the predicted probabilities calculated from model 1 and model 3

CEM radiomics features have been investigated before. Studies have found that the radiomics features within the tumor can contribute to the diagnosis [13–18] and characterization [40, 41, 43] of BCs or the prediction of axillary lymph node metastasis [42]. Considering that different types of BCs have diverse tumor microenvironments and prognoses, it would be interesting to investigate whether the peritumoral radiomics features in CEM images have predictive value in these aspects.

There are several limitations of our study. First, this retrospective study had a relatively small dataset. Therefore, we resplit the dataset 100 times to illustrate the stability and robustness of the model performance. Although the results are promising, a larger, prospective study cohort is needed to further

Table 4 Mean area under the receiver operating characteristic curve (AUC) values of the radiomics models

Radiomics models	Training set		Testing set	
	Mean ± SD	Median (Q1, Q3)	Mean ± SD	Median (Q1, Q3)
Model 1: lesion (L)	0.980 ± 0.014	0.982 (0.972,0.992)	0.930 ± 0.021	0.932 (0.919,0.946)
Model 2: annular perilesional ROI of 1 mm (P1)	0.982 ± 0.014	0.985 (0.972,0.992)	0.936 ± 0.019	0.934 (0.927,0.948)
Model 3: annular perilesional ROI of 3 mm (P3)	0.982 ± 0.013	0.984 (0.973,0.993)	0.940 ± 0.018	0.941 (0.927,0.953)
Model 4: annular perilesional ROI of 5 mm (P5)	0.979 ± 0.015	0.981 (0.969,0.992)	0.929 ± 0.018	0.930 (0.918,0.943)
Model 5: lesion + perilesional ROI of 1 mm (LP1)	0.973 ± 0.021	0.977 (0.963,0.988)	0.902 ± 0.031	0.908 (0.891,0.921)
Model 6: lesion + perilesional ROI of 3 mm (LP3)	0.962 ± 0.024	0.964 (0.950,0.980)	0.892 ± 0.028	0.897 (0.872,0.910)
Model 7: lesion + perilesional ROI of 5 mm (LP5)	0.963 ± 0.023	0.967 (0.950,0.979)	0.901 ± 0.023	0.899 (0.885,0.917)
Model 8*: model 1 + model 3	0.988 ± 0.011	0.989 (0.981,0.999)	0.963 ± 0.013	0.967 (0.957,0.973)

*Model 8 was constructed by combining the predicted probabilities calculated from model 1 and model 3

SD standard deviation

validate the prediction efficiency of the models. Second, we acknowledge a higher prevalence of malignant lesions in our study (54.7%), which implies potential patient selection bias. However, a balanced dataset is also important for developing radiomics classification models. Third, although the perilesional region was generated automatically by the postprocessing workstation, the lesion contours were delineated manually in this study. An automated or semiautomated segmentation method may have better reproducibility. In this study, we calculated the intraobserver and interobserver ICCs, and the results were favorable, which indicates acceptable reproducibility for manual segmentation. Fourth, due to the inherent characteristics of the CEM technique, we extracted two-dimensional radiomics features, which may have lost some lesion information compared to three-dimensional features. However, the results showed that two-dimensional-based features can also demonstrate good performance in classifying breast lesions.

In conclusion, our study found that an annular perilesional region of 3 mm in CEM images is useful to differentiate benign and malignant breast lesions. Adding annular perilesional information to the radiomics model built on the lesion information may improve the diagnostic performance.

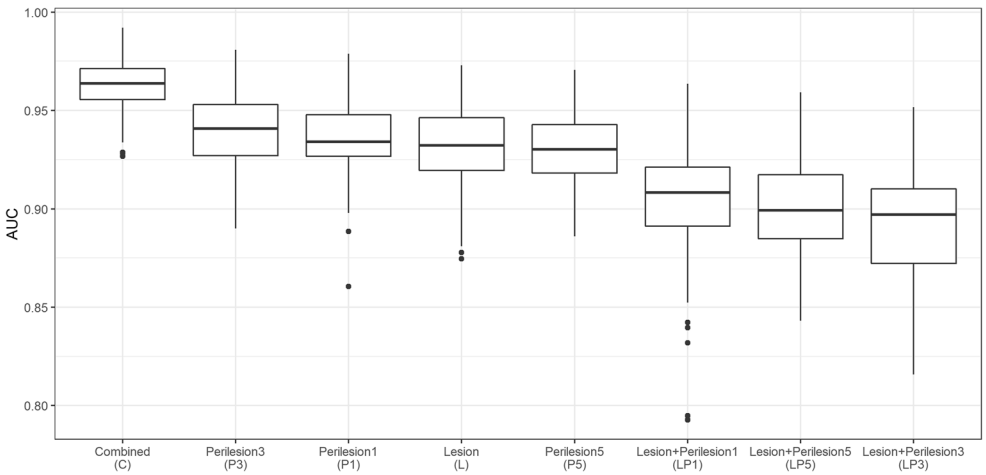

Figure 6 Boxplots of the mean area under the receiver operating characteristic curve (AUC) values of the eight radiomics models in the testing set. Model 1 (L): lesion ROI. Model 2 (P1): annular perilesional ROI of 1 mm. Model 3 (P3): annular perilesional ROI of 3 mm. Model 4 (P5): annular perilesional ROI of 5 mm. Model 5 (LP1): lesion + perilesional ROI of 1 mm. Model 6 (LP3): lesion + perilesional ROI of 3 mm. Model 7 (LP5): lesion + perilesional ROI of 5 mm. The combined model (model 8) was constructed by combining the predicted probabilities calculated from model 1 and model 3

Supplementary Information The online version contains supplementary material available at https://doi.org/10.1007/s00330-021-08134-y.

Acknowledgements The authors are thankful to Boran Pang, MD, for providing technical support and inspiration in experimental design. Permission was obtained from him. We also acknowledge funding and support from the National Natural Science Foundation of China (NSFC 82071878), the Shanghai Anticancer Association FLIGHT PROJECT (SACA-AX-201903), the Shanghai Science and Technology Foundation (19DZ1930502), and the Clinical Research Plan of SHDC (SHDC2020CR2008A).

Funding This study has received funding from the National Natural Science Foundation of China (NSFC 82071878), the Shanghai Anticancer Association FLIGHT PROJECT (SACA-AX-201903), the Shanghai Science and Technology Foundation (19DZ1930502), and the Clinical Research Plan of SHDC (SHDC2020CR2008A).

Declarations

Guarantor The scientific guarantor of this publication is Prof. Yajia Gu.

Conflict of interest Two of the co-authors (Q.C. and S.D.) are employees of General Electric (GE) Healthcare (Shanghai, China). No other potential conflict of interest relevant to this article has been reported.

Statistics and biometry One of the co-authors (Y.S.) has significant statistical expertise.

Informed consent The patient written informed consent was waived in this study.

Ethical approval Institutional Review Board approval was obtained.

Methodology
- retrospective
- cross sectional study/observational
- single center study

References

1. Lewin JM, Isaacs PK, Vance V, Larke FJ (2003) Dual-energy contrast-enhanced digital subtraction mammography: feasibility. Radiology 229:261–268
2. Jochelson MS, Lobbes MBI (2021) Contrast-enhanced mammography: state of the Art. Radiology 299:36–48
3. Sogani J, Mango VL, Keating D, Sung JS, Jochelson MS (2021) Contrast-enhanced mammography: past, present, and future. Clin Imaging 69:269–279
4. Ghaderi KF, Phillips J, Perry H, Lotfi P, Mehta TS (2019) Contrast-enhanced mammography: current applications and future directions. Radiographics 39:1907–1920
5. Perry H, Phillips J, Dialani V et al (2018) Contrast-enhanced mammography: a systematic guide to interpretation and reporting. AJR Am J Roentgenol 212:222–231
6. Weidner N, Semple JP, Welch WR, Folkman J (1991) Tumor angiogenesis and metastasis–correlation in invasive breast carcinoma. N Engl J Med 324:1–8
7. Weidner N (2004) The importance of tumor angiogenesis: the evidence continues to grow. Am J Clin Pathol 122:675–677
8. Dromain C, Thibault F, Muller S et al (2011) Dual-energy contrast-enhanced digital mammography: initial clinical results. Eur Radiol 21:565–574
9. Mori M, Akashi-Tanaka S, Suzuki S et al (2017) Diagnostic accuracy of contrast-enhanced spectral mammography in comparison to conventional full-field digital mammography in a population of women with dense breasts. Breast Cancer 24:104–110
10. Cheung YC, Lin YC, Wan YL et al (2014) Diagnostic performance of dual-energy contrast-enhanced subtracted mammography in dense breasts compared to mammography alone: interobserver blind-reading analysis. Eur Radiol 24:2394–2403
11. Lambin P, Rios-Velazquez E, Leijenaar R et al (2012) Radiomics: extracting more information from medical images using advanced feature analysis. Eur J Cancer 48:441–446
12. Gillies RJ, Kinahan PE, Hricak H (2015) Radiomics: images are more than pictures, they are data. Radiology 278:563–577
13. Fanizzi A, Losurdo L, Basile TMA et al (2019) Fully automated support system for diagnosis of breast cancer in contrast-enhanced spectral mammography images. J Clin Med 8:891
14. Danala G, Patel B, Aghaei F et al (2018) Classification of breast masses using a computer-aided diagnosis scheme of contrast enhanced digital mammograms. Ann Biomed Eng 46:1419–1431
15. Patel BK, Ranjbar S, Wu T et al (2018) Computer-aided diagnosis of contrast-enhanced spectral mammography: a feasibility study. Eur J Radiol 98:207–213
16. Fusco R, Vallone P, Filice S et al (2019) Radiomic features analysis by digital breast tomosynthesis and contrast-enhanced dual-energy mammography to detect malignant breast lesions. Biomed Signal Proces 53:101568
17. Losurdo L, Fanizzi A, Basile T et al (2019) Radiomics analysis on contrast-enhanced spectral mammography images for breast cancer diagnosis: a pilot study. Entropy 21:1110
18. Lin F, Wang Z, Zhang K et al (2020) Contrast-enhanced spectral mammography-based radiomics nomogram for identifying benign and malignant breast lesions of Sub-1 cm. Front Oncol 10:573630
19. Christiansen A, Detmar M (2011) Lymphangiogenesis and cancer. Genes Cancer 2:1146–1158
20. Grivennikov SI, Greten FR, Karin M (2010) Immunity, inflammation, and cancer. Cell 140:883–899
21. Pagès F, Galon J, Dieu-Nosjean MC et al (2010) Immune infiltration in human tumors: a prognostic factor that should not be ignored. Oncogene 29:1093–1102
22. Ocaña A, Diez-Gónzález L, Adrover E et al (2015) Tumor-infiltrating lymphocytes in breast cancer: ready for prime time? J Clin Oncol 33:1298–1299
23. Chan TS, Shaked Y, Tsai KK (2019) Targeting the interplay between cancer fibroblasts, mesenchymal stem cells, and cancer stem cells in desmoplastic cancers. Front Oncol 9:688
24. Conklin MW, Keely PJ (2012) Why the stroma matters in breast cancer: insights into breast cancer patient outcomes through the examination of stromal biomarkers. Cell Adhes Migr 6:249–260
25. Zhou J, Zhang Y, Chang KT et al (2020) Diagnosis of benign and malignant breast lesions on DCE-MRI by using radiomics and deep learning with consideration of peritumor tissue. J Magn Reson Imaging 51:798–809
26. Zhou Y, Xu J, Liu Q et al (2018) A radiomics approach with CNN for shear-wave elastography breast tumor classification. IEEE Trans Biomed Eng 65:1935–1942
27. Yu Y, Xiao Y, Cheng J, Chiu B (2018) Breast lesion classification based on supersonic shear-wave elastography and automated lesion segmentation from B-mode ultrasound images. Comput Biol Med 93:31–46
28. Klimonda Z, Karwat P, Dobruch-Sobczak K, Piotrzkowska-Wróblewska H, Litniewski J (2019) Breast-lesions characterization using quantitative ultrasound features of peritumoral tissue. Sci Rep 9:7963

29. Sun Q, Lin X, Zhao Y et al (2020) Deep learning vs. radiomics for predicting axillary lymph node metastasis of breast cancer using ultrasound images: don't forget the peritumoral region. Front Oncol 10:53
30. Liu C, Ding J, Spuhler K et al (2019) Preoperative prediction of sentinel lymph node metastasis in breast cancer by radiomic signatures from dynamic contrast-enhanced MRI. J Magn Reson Imaging 49:131–140
31. Braman N, Prasanna P, Whitney J et al (2019) Association of peritumoral radiomics with tumor biology and pathologic response to preoperative targeted therapy for HER2 (ERBB2)-positive breast cancer. JAMA Netw Open 2:e192561
32. Braman NM, Etesami M, Prasanna P et al (2017) Intratumoral and peritumoral radiomics for the pretreatment prediction of pathological complete response to neoadjuvant chemotherapy based on breast DCE-MRI. Breast Cancer Res 19:57
33. D'Orsi CJ, Sickles EA, Mendelson EB et al (2013) ACR BI-RADS® Atlas (5th edition). American College of Radiology, Reston
34. Yushkevich PA, Piven J, Hazlett HC et al (2006) User-guided 3D active contour segmentation of anatomical structures: significantly improved efficiency and reliability. Neuroimage 31:1116–1128
35. Beig N, Khorrami M, Alilou M et al (2019) Perinodular and intranodular radiomic features on lung CT images distinguish adenocarcinomas from granulomas. Radiology 290:783–792
36. Park SH, Han K (2018) Methodologic guide for evaluating clinical performance and effect of artificial intelligence technology for medical diagnosis and prediction. Radiology 286:800–809
37. Bluemke DA, Moy L, Bredella MA et al (2020) Assessing radiology research on artificial intelligence: a brief guide for authors, reviewers, and readers-from the Radiology Editorial Board. Radiology 294:487–489
38. Tibshirani R (1996) Regression shrinkage and selection via the LASSO. J Royal Statist Soc B 58:267–288
39. DeLong ER, DeLong DM, Clarke-Pearson DL (1988) Comparing the areas under two or more correlated receiver operating characteristic curves: a nonparametric approach. Biometrics 44:837–845
40. Marino MA, Pinker K, Leithner D et al (2020) Contrast-enhanced mammography and radiomics analysis for noninvasive breast cancer characterization: initial results. Mol Imaging Biol 22:780–787
41. La Forgia D, Fanizzi A, Campobasso F et al (2020) Radiomic analysis in contrast-enhanced spectral mammography for predicting breast cancer histological outcome. Diagnostics 10:708
42. Mao N, Yin P, Li Q et al (2020) Radiomics nomogram of contrast-enhanced spectral mammography for prediction of axillary lymph node metastasis in breast cancer: a multicenter study. Eur Radiol 30: 6732–6739
43. Marino MA, Leithner D, Sung J et al (2020) Radiomics for tumor characterization in breast cancer patients: a feasibility study comparing contrast-enhanced mammography and magnetic resonance imaging. Diagnostics 10:492
44. Schoppmann SF, Bayer G, Aumayr K et al (2004) Prognostic value of lymphangiogenesis and lymphovascular invasion in invasive breast cancer. Ann Surg 240:306–312
45. Ejlertsen B, Jensen MB, Rank F et al (2009) Population-based study of peritumoral lymphovascular invasion and outcome among patients with operable breast cancer. J Natl Cancer Inst 101:729–735
46. Acerbi I, Cassereau L, Dean I et al (2015) Human breast cancer invasion and aggression correlates with ECM stiffening and immune cell infiltration. Integr Biol 7:1120–1134
47. Uematsu T (2015) Focal breast edema associated with malignancy on T2-weighted images of breast MRI: peritumoral edema, prepectoral edema, and subcutaneous edema. Breast Cancer 22: 66–70
48. Roy DM, Walsh LA (2014) Candidate prognostic markers in breast cancer: focus on extracellular proteases and their inhibitors. Breast Cancer (Dove Med Press) 6:81–91
49. Lu P, Weaver VM, Werb Z (2012) The extracellular matrix: a dynamic niche in cancer progression. J Cell Biol 196:395–406
50. Zhou J, Zhan W, Dong Y, Yang Z, Zhou C (2014) Stiffness of the surrounding tissue of breast lesions evaluated by ultrasound elastography. Eur Radiol 24:1659–1667
51. Shin HJ, Park JY, Shin KC et al (2016) Characterization of tumor and adjacent peritumoral stroma in patients with breast cancer using high-resolution diffusion-weighted imaging: correlation with pathologic biomarkers. Eur J Radiol 85:1004–1011
52. Fan M, He T, Zhang P et al (2018) Diffusion-weighted imaging features of breast tumours and the surrounding stroma reflect intrinsic heterogeneous characteristics of molecular subtypes in breast cancer. NMR Biomed 31:e0189302
53. Fan M, He T, Zhang P, Zhang J, Li L (2017) Heterogeneity of diffusion-weighted imaging in tumours and the surrounding stroma for prediction of Ki-67 proliferation status in breast cancer. Sci Rep 7:2875
54. Cheon H, Kim HJ, Kim TH et al (2018) Invasive breast cancer: prognostic value of peritumoral edema identified at preoperative MR imaging. Radiology 287:68–75
55. Chen JH, Zhang Y, Chan S, Chang RF, Su MY (2018) Quantitative analysis of peri-tumor fat in different molecular subtypes of breast cancer. Magn Reson Imaging 53:34–39
56. Kim SG, Freed M, Leite APK et al (2017) Separation of benign and malignant breast lesions using dynamic contrast enhanced MRI in a biopsy cohort. J Magn Reson Imaging 45:1385–1393
57. Li H, Mendel KR, Lan L, Sheth D, Giger ML (2019) Digital mammography in breast cancer: additive value of radiomics of breast parenchyma. Radiology 291:15–20
58. Ding J, Chen S, Serrano SM, et al (2020) Optimizing the peritumoral region size in radiomics analysis for sentinel lymph node status prediction in breast cancer. Acad Radiol 4:1–6